Report: 2025 SCEC Proposal 25322: A Physics-Based Approach for Estimating a Statewide California 3-D Velocity and Strain Rate Field using GNSS and InSAR Data

Principal Investigator: William Holt

Abstract

We present a physics-based framework for estimating a statewide three-dimensional (3-D) velocity and strain-rate field for California through the joint inversion of Global Navigation Satellite System (GNSS) and Interferometric Synthetic Aperture Radar (InSAR) data. Unlike traditional kinematic approaches, our method is grounded in horizontal force-balance equations, where basis functions represent responses to body-force rate inputs equivalent to the vertical derivative of horizontal shear stress (VDoHS) rates. This formulation enables simultaneous estimation of surface velocities, horizontal strain rates, and subsurface force-rate distributions, providing new constraints on fault mechanics, including slip rates and locking depths.

Application to Southern California reveals detailed spatial variability in deformation across major fault systems, including the San Andreas, San Jacinto, and Imperial faults. The results highlight strong transpressional deformation in the Big Bend region, localized zones of compression and extension, and significant strain partitioning across fault networks. The model successfully reproduces observed GNSS velocities and InSAR line-of-sight displacements, demonstrating the robustness of the joint inversion approach.

By extending the analysis to depth, we infer three-dimensional strain accumulation patterns and identify zones of mid-crustal convergence and potential crustal thickening beneath mountain ranges. Comparisons with earthquake-derived moment tensors show consistency in strain orientations, supporting the validity of the depth-dependent framework. Additionally, analysis of spatial gradients of force-rate fields reveals characteristic signatures of elastic fault locking and provides a new physical lens for imaging interseismic deformation.

Overall, this study advances our ability to integrate geodetic datasets within a physics-based framework, offering improved insights into crustal deformation processes and enhancing our understanding of earthquake hazard in California.

1.Introduction

Numerous studies have examined interseismic deformation using geodetic methods, particularly GPS (Bird, 2009; Bourne et al., 1998; Chuang & Johnson, 2011; Evans, 2018; Evans et al., 2015, 2015; Guns et al., 2024; Johnson, 2013, 2024; Johnson & Segall, 2004; Lindsey & Fialko, 2013, 2013; McGill et al., 2015; Meade & Hager, 2005, 2005; Pollitz, 2003; Pollitz & Nyst, 2004; Savage & Burford, 1973; Smith & Sandwell, 2004; Smith-Konter et al., 2011; Tong et al., 2014; Zeng & Shen, 2016, 2014). We present a physics-based joint analysis of GNSS and InSAR that not only provides surface 3-D velocity, horizontal strain rates, and fault characteristics

(slip rates and locking depths) but can also provide information about strain accumulation at depth. Observations from large earthquakes—including the El Mayor-Cucapah event—show that rupture geometry often changes with depth, in strike, dip, and rake (e.g., Yamashita et al., 2022). By estimating depth-dependent three-dimensional strain accumulation rates, we aim to constrain how strain orientations evolve with depth, thereby improving forecasts of rupture geometries in future events.

The physics-based approach taken here, where basis functions represent a force-balance solution response to body force rate equivalent input, is like methods outlined by Haines et al. (2015), Haines & Wallace (2020), and Sandwell & Wessel (2016). A difference is that the potentials we use are integrals of the force rates. For the elastic case these force rates are equivalent to the vertical derivative of horizontal shear stress (VDoHS) rates (Haines et al., 2015). The force-balance solutions involving velocities and strain rates are responses to distributions of force rate couples (Figure 1). It is possible, therefore, to use our 3-D velocity field, strain rates, and force rate distributions to provide additional insights into the dynamics of the interseismic field, including fault locking depths and slip rates (Haines et al., 2015).

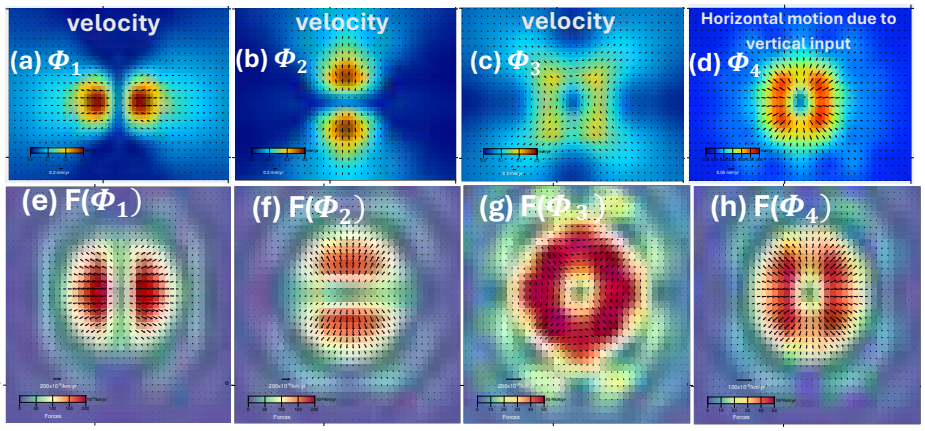

Figure 1. (a)-(d) response functions of velocity and force rates (e)-(h) in response to input potentials.

We present a California case study demonstrating the successful integration of GNSS and InSAR through joint inversion using a physics-based approach to obtain 3-D velocity and strain rate fields.

2.0 Method

Our approach involves solutions to the horizontal force balance equations (expressed in terms of stress rates) on the surface of a sphere in response to body force rate inputs (Fig. 1). In spherical coordinates the effective body force rate term is the vertical derivative of horizontal shear stress (VDoHS) rate:

$$\dot{f}_{\phi} = -\frac{1}{r\cos\theta}\frac{\partial}{\partial\phi}(\mu\dot{\varepsilon}_{\phi\phi} - \mu\dot{\varepsilon}_{\theta\theta}) + \frac{1}{r}4\mu\dot{\varepsilon}_{\phi\theta}\tan\theta - \frac{\partial}{r\,\partial\theta}(2\mu\dot{\varepsilon}_{\phi\theta}) - \frac{1}{r\cos\theta}\frac{\partial}{\partial\phi}\{(3\mu(\dot{\varepsilon}_{\phi\phi} + \dot{\varepsilon}_{\theta\theta})\}$$

$$\dot{f}_{\theta} = \frac{\partial}{r\,\partial\theta}(\mu\dot{\varepsilon}_{\phi\phi} - \mu\dot{\varepsilon}_{\theta\theta}) - \frac{2}{r}(\mu\dot{\varepsilon}_{\phi\phi} - \mu\dot{\varepsilon}_{\theta\theta})\tan\theta - \frac{1}{r\cos\theta}\frac{\partial}{\partial\phi}(2\mu\dot{\varepsilon}_{\phi\theta}) - \frac{\partial}{r\,\partial\theta}\{(3\mu(\dot{\varepsilon}_{\phi\phi} + \dot{\varepsilon}_{\theta\theta})\} \quad (1)$$

where ϕ is the longitude; θ is the latitude; $\dot{\varepsilon}_{\phi\phi}$, $\dot{\varepsilon}_{\theta\phi}$, and $\dot{\varepsilon}_{\theta\theta}$ are the horizontal strain rates, and μ is the shear modulus (Finzel et al., 2015; Haines et al., 2015; Vashishtha et al., 2024 a,b).

3.0 High-Resolution Strain Rates and Force Rate Mapping: Southern California

Our joint inversion of GNSS and InSAR data provides a high-fidelity, regional 3D velocity field

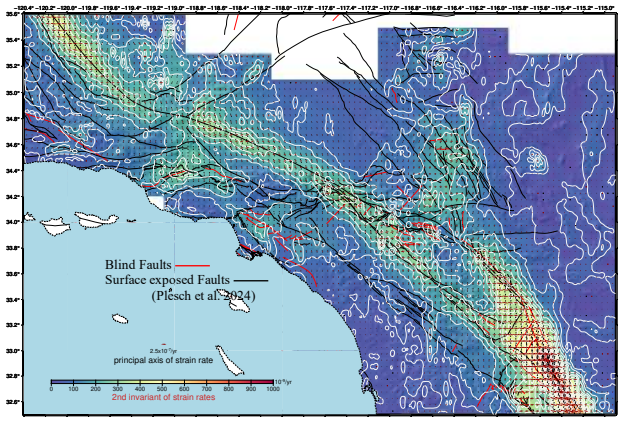

Figure 2. Estimated Horizontal strain rate field from the Joint Inversion. Background field is the second invariant of strain rate and the principal axes of strain rates are also shown.

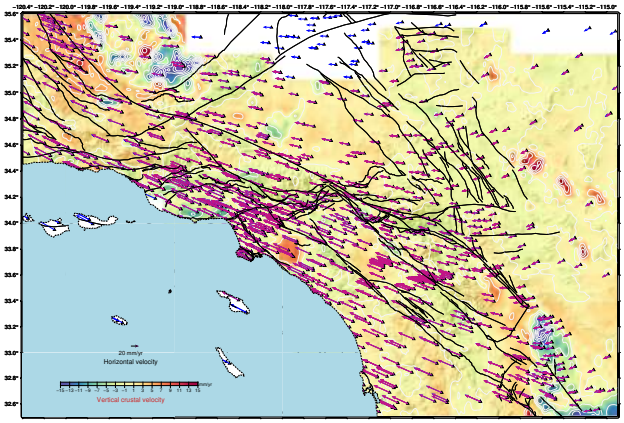

Figure 3. Input GNSS velocities from Blewitt et al. 2016 (NGL's MIDAS) and Zeng (2022) (orange arrows) in ITRF14 frame. Model velocities from the Joint Inversion are gray arrows. Vertical velocity is in color background.

and subsequent Vertical Derivative of Horizontal Shear Stress (VDoHS) rate estimates (Figures 2-5). This solution offers a rare combination of vast spatial coverage and high-resolution detail, allowing for the identification of complex deformation patterns across the entire Southern California plate boundary zone.

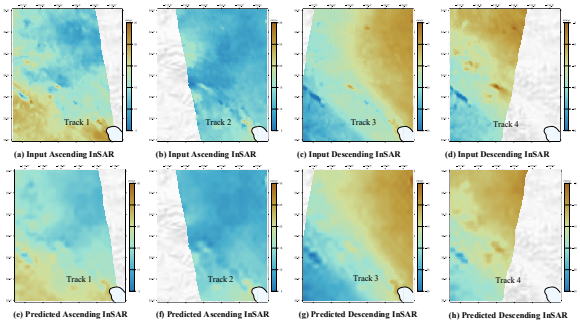

Figure 4. (a)-(c) Input InSAR data obtained from Xu et al. 2021. (e)-(h) prediction of InSAR data using the joint inversion

Summary of Key Insights:

- **Off-Fault Deformation Signals:** The model resolves significant off-fault deformation in regions adjacent to major along-strike variations in strain rates or slip rates. These signals highlight how stress is redistributed beyond the primary fault traces in complex tectonic zones.

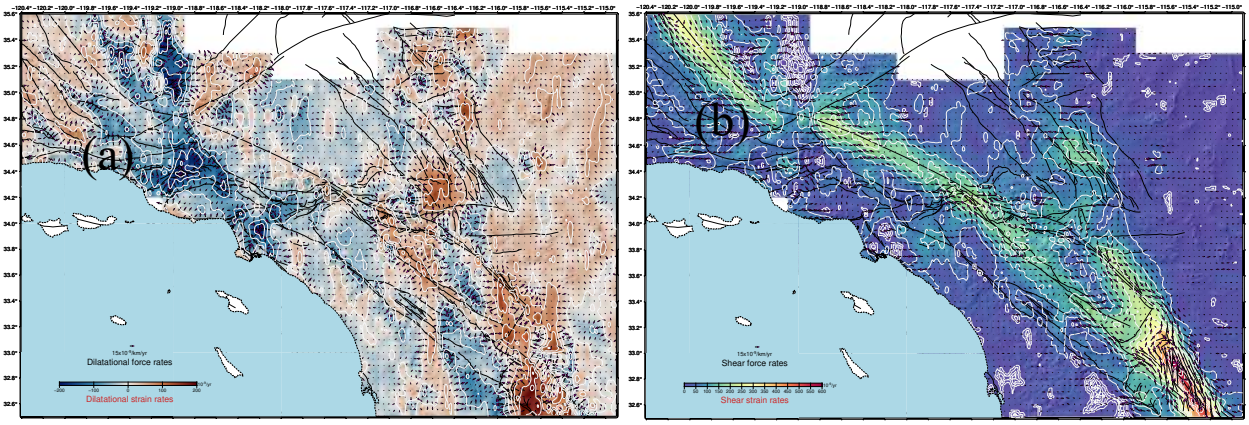

Figure 5. (a) Dilatational and (b) Shear component of force rates (Vertical derivative of horizontal shear stress rates (VDoHS)) at the surface obtained from the Joint Inversion of GNSS and InSAR.

- **Multi-Scale Resolution:** The solution captures the heterogeneous transition between strike-slip and compressional/extensional regimes with high precision.
- **Force Rate Gradients:** The VDoHS estimates quantify the vertical gradients of horizontal shear stress rates. This approach reveals a wealth of localized details in the force rate field, providing a more granular view of crustal loading than traditional 1D or 2D models. This approach for example provides insights into the source of off-fault deformation.

Research Impact:

The strength of this inversion lies in its ability to be "zoomed in" on any sub-region to reveal segment-level details of force redistribution and off-fault strain rates. While this report provides the regional context, the immense detail captured here—specifically the interplay between primary structures and secondary deformation—will be the focus of our forthcoming publication and detailed segment-specific analysis.

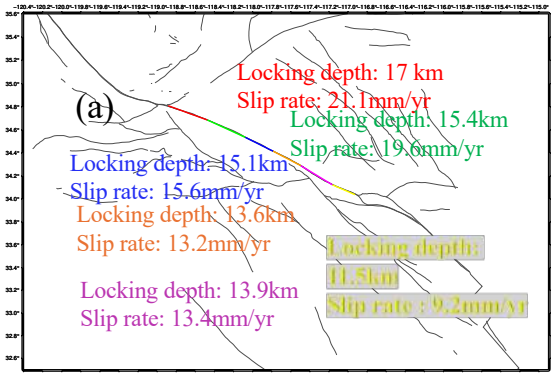

Figure 6. (a) Fault properties of slip rate and locking depth estimated for the Big Bend portion of San Andreas Fault using strain rates and force rates obtained from the Joint Inversion. The segments where rates and locking depths have been obtained are color-coded along with their respective fault properties.

4.0 Fault characteristics

For both strike-slip and dip-slip faults, the widths of the strain-rate and VDoHS rate peaks are proportional to the locking depth. Strain-rate and VDoHS rate peak amplitudes depend differently on locking depth. The relation for vertical strike slip faults is

Locking depth $= 1.3\frac{\dot{e}_{xy}}{\dot{f}_y}$ and Slip rate $= 8.15\frac{\dot{e}_{xy}{}^2}{\dot{f}_y}$. Here $\dot{e}_{xy}$ is obtained by rotating the

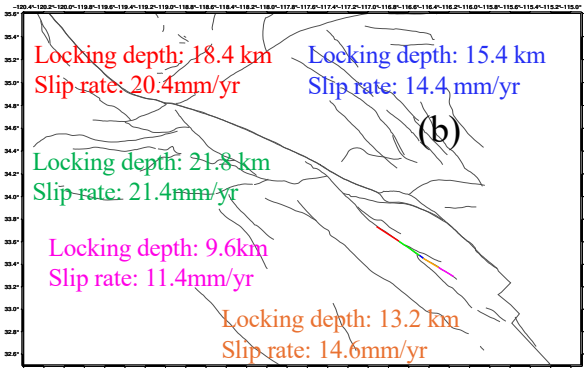

Figure 6. (b) Same as Figure 6. (a) with properties for segments of the San Jacinto Fault.

strain rate tensor, with one prime axis parallel to strike, and $\dot{\mathbf{f}}$ is projected along the strike direction (for strike-slip faults) as shown in Figure 6, and along dip direction (for dip-slip faults). The SCEC Community Fault Model 7.0 (Plesch et al. 2024) provides information on expected fault strike, which we have used to obtain the fault locking depth and slip rates in Figure 6.

5.0 Treatment of creeping sections

We have built creep basis functions involving step offsets to investigate creep rates along zones where InSAR LOS clearly delineate creep. The treatment of creep should improve estimates for velocity gradients adjacent to creeping sections and should also improve the fit to InSAR LOS. The creep function tapers off towards ends to avoid instabilities and extreme strains. The next step is to incorporate this formulation into the G matrix and invert for creep rates.

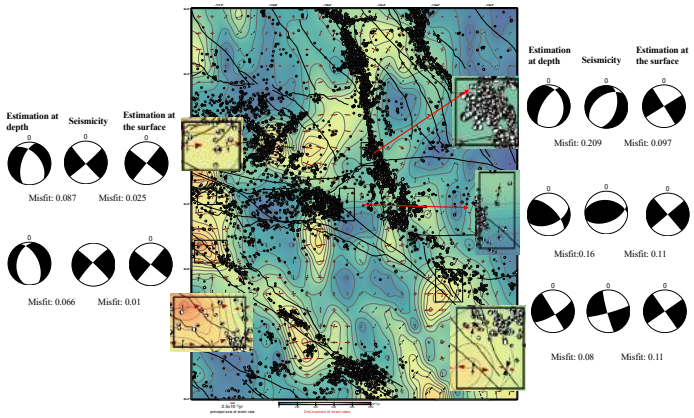

Figure 7. Comparison of strain tensor with the Kostrov summed moment tensors (Cheng et al. 2023) for both surface and at depth (10 km).

6.0 Strain rates and velocities with depth

We reconstruct gradients of velocity as a function of depth by assuming the linear relationship $\frac{\partial u_i}{\partial x_j} = a_k z + b_k$. The b-coefficients are determined by the horizontal gradients in the vertical velocities, known from the joint inversion, since at z=0, $\frac{\partial u_z}{\partial x} = -\frac{\partial u_x}{\partial z}$ and $\frac{\partial u_z}{\partial y} = -\frac{\partial u_y}{\partial z}$. Our force-balance treatment provides values for $\frac{\partial \dot{\epsilon}_{xz}}{\partial z}$ and $\frac{\partial \dot{\epsilon}_{yz}}{\partial z}$ at the surface (from the VDoHS rates), and this constraint, together with the assumption that $\frac{\partial \dot{\omega}_{iz}}{\partial z} = 0$, yields the a-coefficients. Thus, strain rates can be determined with depth. Integration of the velocity gradient equations with respect to depth yields horizontal and vertical velocities as a function of depth.

$$u_x(z) = \frac{\partial \varepsilon_{xz}}{\partial z}\frac{z^2}{2} + (-\frac{\partial u_z(0)}{\partial x})z + u_x(0) \quad (2)$$

$$u_y(z) = \frac{\partial \varepsilon_{yz}}{\partial z}\frac{z^2}{2} + (-\frac{\partial u_z(0)}{\partial y})z + u_y(0) \quad (3)$$

Some care must be taken when dealing with the gradients in vertical velocity, since these are influenced by groundwater processes. We apply a smoothing to the gradient field of vertical velocity to damp out higher amplitude and shorter wavelength variations that can be attributed to groundwater effects. Using this approach, we are finding significant agreement in depth predictions of strain orientations with that inferred from the moment tensors of earthquakes (Cheng et al., 2023). A Kostrov (1974) moment tensor summation of data from this catalog can yield estimates of the 3-D strain field as a function of depth. Model results will be tested through comparisons with the moment tensors of 716,513 earthquakes provided by the Cheng et al. (2023) catalogue. We quantify the misfit between the normalized predicted strain tensor field (6 independent elements) with the Kostrov summed seismic moment tensors (for a given volume at depth), using the objective measures (Flesch et al., 2007; Ghosh et al., 2013). This analysis tests the validity of our linear assumption for velocity gradients with depth. We also conduct a null hypothesis test, assuming no depth-dependence to velocity, and compare the predictions from the surface field alone to the seismic moment tensors at depth (as done for Figure 7).

7.0 Mid crustal deformation

Beneath the San Bernardino, Little San Bernadino, Mecca Hills, and Santa Rosa ranges along the Southern San Andreas and San Jacinto fault zone sections, our depth-dependent velocity and strain rate field yields convergence (Figure 8) of force rate vectors. Extrapolating surface gradients with depth holds implications for possible crustal thickening at greater depths beneath

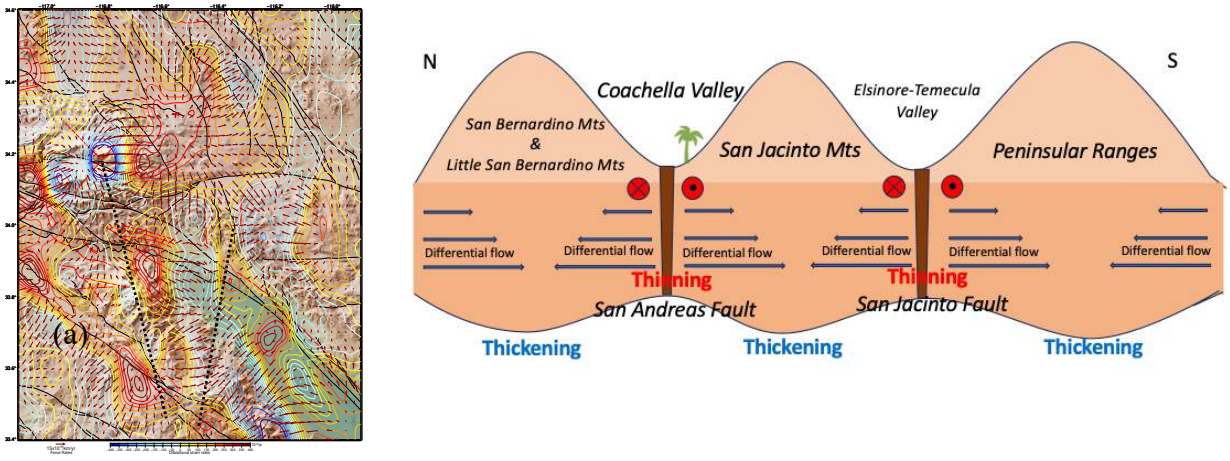

Figure 8. (a) Mid crustal deformation inferred from extrapolation of VDoHS (surface values plotted as vectors) using equations (2) and (3). The contour lines show mid-crustal dilatation strain rates. Cartoon on the right shows implications for the dashed profiles in Figure 8 (a), with crustal thinning within valleys containing the major strike-slip faults and crustal thickening beneath the ranges.

these ranges, which would cause long-term uplift. These patterns were not as obvious from the surface strain rate fields, but can be seen in the VDoHS patterns (Figure 8 a) and further arise from our depth-dependent velocity and strain modeling, described below. Recent Moho depth estimates (Sui et al., 2023) confirm thicker crust below zones of mid-crustal convergence.

8.0 Implications for along-strike slip-rate variation in force rate field

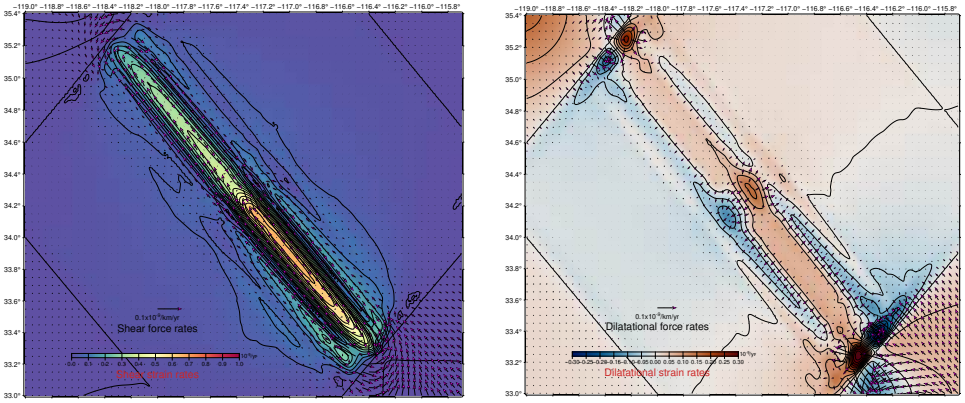

Figure 9 Along strike variation in slip rate manifests as zones of compression and extension at the junction of change. (a) slip rate change as seen in shear force rate space vectors and background shear strain rates and (b) zones of compression (converging force rate vectors) and extension (diverging force rate vectors) with background of dilatational strain rates

We constructed a synthetic strike slip fault system to explore the implications of along-strike slip variations using a force-balance approach. Models show zones of compression and extension at the junction of slip rate change. These along-strike slip rate changes induce force rates oriented at a high angle to the strike-slip fault, which manifest as off-fault deformation involving both extension and contraction. This is much like what we see along stretches of the San Andreas and San Jacinto Fault zones, as elucidated through our force-balance based approach. We hypothesize that on geologic time scales these patterns of extension and compression are responsible, in part, for the development of topography we see today in this plate boundary zone system. Fialko et al. (2005) takes this topography along the San Andreas Fault and works backward, showing that the topographic load perturbs the vertical stress enough to rotate a non-vertical fault, and uses that rotation to infer a crustal differential stress of ~50 MPa.

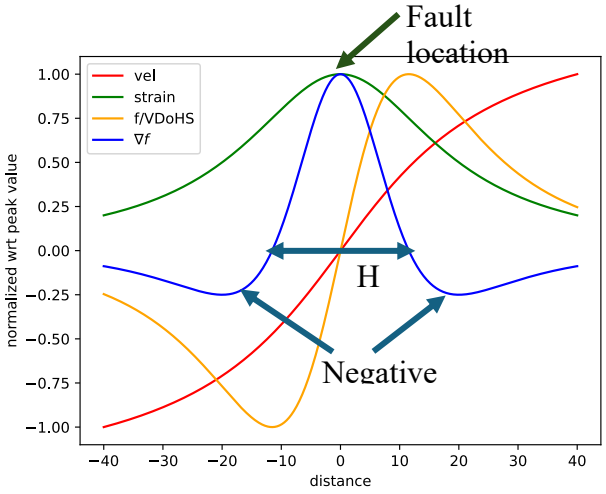

Figure 10 1-dimensional functional forms of horizontal component surface velocities, strain rates, VDoHS rates, and gradients of force rates on vertical strike slip fault

9.0 Spatial gradients of force rate and implication for fault related deformation field

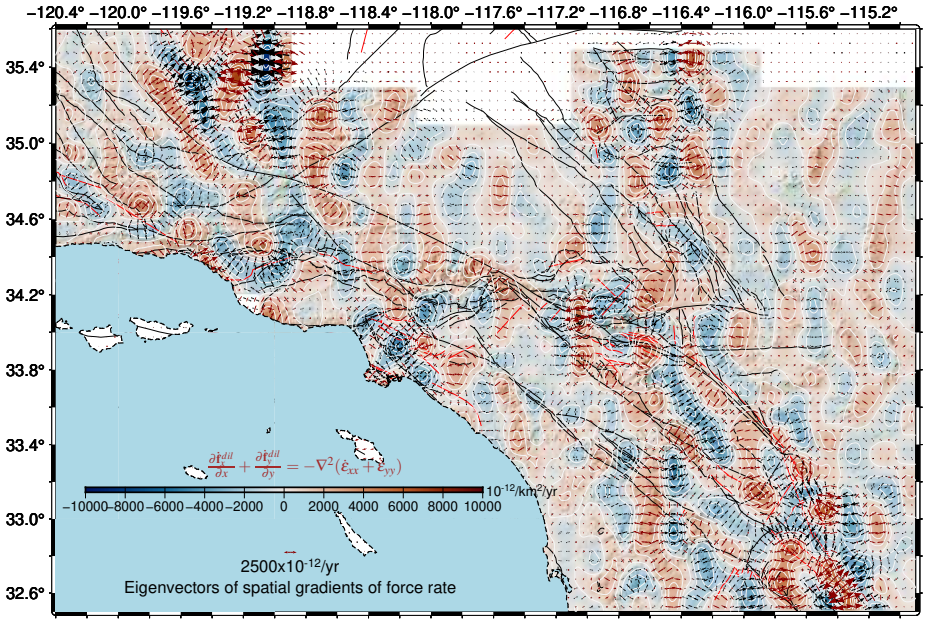

Figure 11 Contoured background shows divergence of spatial gradients of dilatational component of force rate field. Eigenvectors of spatial gradients of force rates, equal to directions of maximum (convergence rate) and minimum (divergence rate) in force rate gradients.

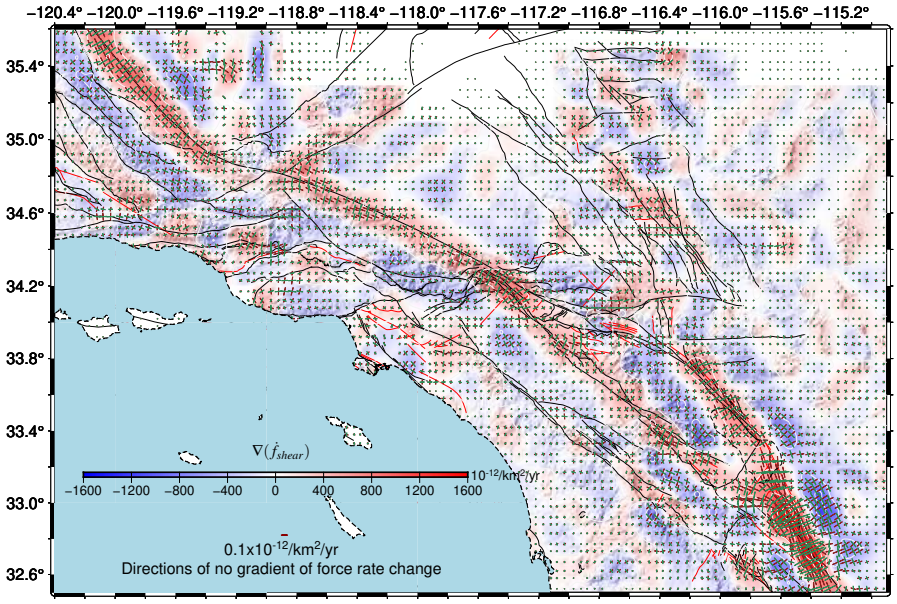

Figure 12. Background shows the shear component of the spatial gradient field of force rates G1_F = (dFx/dx – dFy/dy). The bars show directions along which the spatial gradients in force rate are zero. These directions align with major strike-slip structures and their magnitudes (length of lines) also predict location of maximum shear along with the sense of slip (right-lateral or left-lateral) on those faults.

We are analyzing the force-rate flux field, F = (Fx, Fy), which represents the vertical gradients of shear stress that balance the horizontal divergence of in-plane stresses. The Jacobian of F (∇F) describes the curvature of stress transfer between vertical and horizontal stress gradients. For the shear component, this curvature organizes into a clear "Mexican-hat" pattern: a central lobe of one sign directly over the transform fault, flanked by two lobes of opposite sign (Figure 10). The width of the central lobe (Hf) scales with locking depth (D ≈0.87Hf), providing a way to image elastic locking directly, without slip inversion. The eigenvectors of ∇F lie approximately 45° to strike, consistent with principal strain-rate orientations, while directions of near-

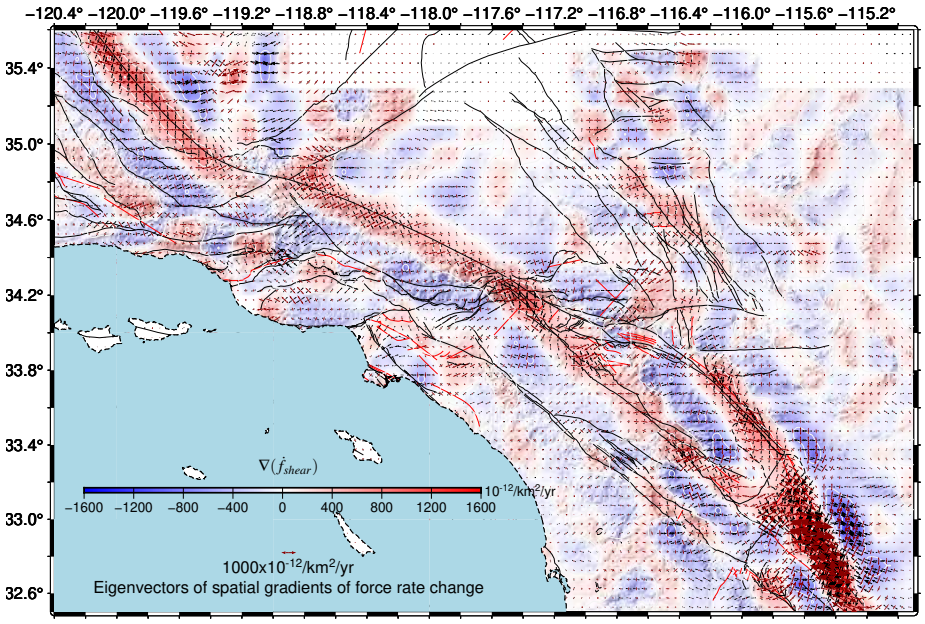

Figure 13 Background shows the shear component of the spatial gradient field of force rates G1_F = (dFx/dx – dFy/dy). The arrows show eigenvectors of spatial gradient of force rate change, as in Figure 11. The width of the belt of positive G1_F (labeled Hf in Figure 12) that runs parallel to the major strike-slip transform faults is proportional to fault locking depth. Note that double lobes of opposite sign, on either side of the positive anomaly, is a signature of elastic locking on major transform faults.

zero curvature run along strike. In contrast, the dilatational component is more complex: it tends to converge beneath mountains and diverge away from transform valleys, showing how locking, and along-strike variations in locking, couples into larger-scale lithospheric stresses that lead to off-fault deformation in the form of dilatation. In this way, ∇F provides a new physical lens on interseismic deformation: it directly images the curvature of stress transfer, highlighting fault-parallel locking in shear and broader convergence /divergence in dilatation.

In Figure 11 we show ∇F associated with the dilatational part of the field, along with the eigenvectors of this field, which highlight directions of maximum shortening/extensional rate of strain. Note from Figure 11 that these directions are often at high angles to the strikes of the major transform structures. In many cases the directions of maximum rate of change in shortening agree with the directions of actual shortening inferred from fold and thrust belt geometries adjacent to the major transform structures (e.g., Mecca Hills, Bergh et al., 2019). Blue regions in Figure 11 show expected zones of peak convergence rate and the hotter colors show areas of peak crustal extension rate.

Figures 12 and 13 show ∇F linked to the transform (shear) part of the field, and it provides a way to image elastic locking without slip inversion. It highlights fault-parallel locking. The double lobes of opposite sign, on either side of the positive anomaly, is a signature of elastic locking on the major transform faults (San Andreas and San Jacinto). We plot in Figure 12 the directions along which ∇F is zero and find that these directions align with major right-lateral and left-lateral transform faults, and predict the sign of movement on these faults. In Figure 13 we plot the eigenvector directions of ∇F (shear). The geometrical alignment of the ∇F fields with mapped fault patterns strongly suggests that noise amplification is not dominating our force-balance based solution. The patterns of F and ∇F show consistent physical meaning (lobes, orientations,

convergence/divergence patterns) rather than random artifacts, which holds significant promise for providing new insights into the 3-D dynamics of this complex transform system.

10.0 Intellectual Merit and Broader Impact

We combine the strengths of GNSS and InSAR using the joint inversion to overcome their spatial and directional limitations respectively. We use this joint inversion algorithm to provide an estimate of a time-averaged strain rate field (15-year average), rotation rates, and vertical gradients of horizontal shear stress (VDoHS) rates. We also develop a method to determine the velocity field and full strain rate tensor at depth within the crust. We investigate the gradients of force rates (divergence and shear), eigenvectors of these gradient fields, and directions of zero change in these gradient fields. We show that these gradient fields yield insights into the dynamics of the elastic field including fault locking depths, slip rates, maximum shear and predictions of peak shortening rates, their orientations, and their locations.

Our goal is to contribute our final Statewide California model products, together with the algorithm, to the SCEC CGM. We also plan to participate in the Community Velocity Model exercise to do a comparative study with other groups working on different methods for jointly inverting GNSS and InSAR archived in the CGM.

During this funding period we have applied our algorithm to California, which was presented at the SCEC annual meeting in 2025 and published as (Kim et al., 2026). This effort to obtain an optimal secular field will refine the method for addressing time-dependent changes in strain. Expected products include two published peer-reviewed papers in which all methods, results, scripts and codes will be available in supplementary.

11.0 References

Bergh, S. G., Sylvester, A. G., Damte, A., & Indrevær, K. (2019). Polyphase kinematic history of transpression along the Mecca Hills segment of the San Andreas fault, southern California. *Geosphere*, *15*(3), 901–934. https://doi.org/10.1130/GES02027.1

Bird, P. (2009). Long-term fault slip rates, distributed deformation rates, and forecast of seismicity in the western United States from joint fitting of community geologic, geodetic, and stress direction data sets. *Journal of Geophysical Research: Solid Earth*, *114*(B11), 2009JB006317. https://doi.org/10.1029/2009JB006317

Bourne, S. J., England, P. C., & Parsons, B. (1998). The motion of crustal blocks driven by flow of the lower lithosphere and implications for slip rates of continental strike-slip faults. *Nature*, *391*(6668), 655–659. https://doi.org/10.1038/35556

Cheng, Y., Hauksson, E., & Ben-Zion, Y. (2023). Refined Earthquake Focal Mechanism Catalog for Southern California Derived With Deep Learning Algorithms. *Journal of Geophysical Research: Solid Earth*, *128*(2), e2022JB025975. https://doi.org/10.1029/2022JB025975

Chuang, R. Y., & Johnson, K. M. (2011). Reconciling geologic and geodetic model fault slip-rate discrepancies in Southern California: Consideration of nonsteady mantle flow and lower crustal fault creep. *Geology*, *39*(7), 627–630. https://doi.org/10.1130/G32120.1

Evans, E. L. (2018). A Comprehensive Analysis of Geodetic Slip-Rate Estimates and Uncertainties in California. *Bulletin of the Seismological Society of America*, *108*(1), 1–18. https://doi.org/10.1785/0120170159

Evans, E. L., Loveless, J. P., & Meade, B. J. (2015). Total variation regularization of geodetically and geologically constrained block models for the Western United States. *Geophysical Journal International*, *202*(2), 713–727. https://doi.org/10.1093/gji/ggv164

Fialko, Y., Rivera, L., & Kanamori, H. (2005). Estimate of differential stress in the upper crust from variations in topography and strike along the San Andreas fault. *Geophysical Journal International*, *160*(2), 527–532. https://doi.org/10.1111/j.1365-246X.2004.02511.x

Finzel, E. S., Flesch, L. M., Ridgway, K. D., Holt, W. E., & Ghosh, A. (2015). Surface motions and intraplate continental deformation in Alaska driven by mantle flow. *Geophysical Research Letters*, *42*(11), 4350–4358. https://doi.org/10.1002/2015GL063987

Flesch, L. M., Holt, W. E., Haines, A. J., Wen, L., & Shen-Tu, B. (2007). The dynamics of western North America: Stress magnitudes and the relative role of gravitational potential energy, plate interaction at the boundary and basal tractions. *Geophysical Journal International*, *169*(3), 866–896. https://doi.org/10.1111/j.1365-246X.2007.03274.x

Ghosh, A., Holt, W. E., & Wen, L. (2013). Predicting the lithospheric stress field and plate motions by joint modeling of lithosphere and mantle dynamics. *Journal of Geophysical Research: Solid Earth*, *118*(1), 346–368. https://doi.org/10.1029/2012JB009516

Guns, K., Sandwell, D., Xu, X., Bock, Y., Yong, L. W., & Smith-Konter, B. (2024). Seismic Moment Accumulation Rate From Geodesy: Constraining Kostrov Thickness in Southern California. *Journal of Geophysical Research: Solid Earth*, *129*(5), e2023JB027939. https://doi.org/10.1029/2023JB027939

Haines, A. J., Dimitrova, L. L., Wallace, L. M., & Williams, C. A. (2015). *Enhanced Surface Imaging of Crustal Deformation: Obtaining Tectonic Force Fields Using GPS Data*. Springer International Publishing. https://doi.org/10.1007/978-3-319-21578-5

Haines, A. J., & Wallace, L. M. (2020). New Zealand-Wide Geodetic Strain Rates Using a Physics-Based Approach. *Geophysical Research Letters*, *47*(1), e2019GL084606. https://doi.org/10.1029/2019GL084606

Johnson, K. M. (2013). Slip rates and off-fault deformation in Southern California inferred from GPS data and models. *Journal of Geophysical Research: Solid Earth*, *118*(10), 5643–5664. https://doi.org/10.1002/jgrb.50365

Johnson, K. M. (2024). Disagreements in Geodetically Inferred Strain Rates in the Western US With Stress Orientations and Geologic Moment Rates. *Journal of Geophysical Research: Solid Earth*, *129*(4), e2023JB027472. https://doi.org/10.1029/2023JB027472

Johnson, K. M., & Segall, P. (2004). Viscoelastic earthquake cycle models with deep stress-driven creep along the San Andreas fault system. *Journal of Geophysical Research: Solid Earth*, *109*(B10), 2004JB003096. https://doi.org/10.1029/2004JB003096

Kim, J., Vashishtha, M., Holt, W. E., Murray, K. D., & Lohman, R. B. (2026). A Joint Inversion Algorithm of GNSS and InSAR for Continuous 3-D Surface Velocities and Associated Horizontal Strain Rate Field. *Geochemistry, Geophysics, Geosystems*, *27*(3), e2025GC012682. https://doi.org/10.1029/2025GC012682

Kostrov, V. V. (1974). Seismic moment and energy of earthquakes, and seismic flow of rock (in Russian). Izvestiya Academia of Sciences. USSR Physics of the Solid Earth, 1, 23–44.

Lindsey, E. O., & Fialko, Y. (2013). Geodetic slip rates in the southern San Andreas Fault system: Effects of elastic heterogeneity and fault geometry. *Journal of Geophysical Research: Solid Earth*, *118*(2), 689–697. https://doi.org/10.1029/2012JB009358

McGill, S. F., Spinler, J. C., McGill, J. D., Bennett, R. A., Floyd, M. A., Fryxell, J. E., & Funning, G. J. (2015). Kinematic modeling of fault slip rates using new geodetic velocities from a transect across the Pacific-North America plate boundary through the San Bernardino Mountains, California. *Journal of Geophysical Research: Solid Earth*, *120*(4), 2772–2793. https://doi.org/10.1002/2014JB011459

Meade, B. J., & Hager, B. H. (2005). Block models of crustal motion in southern California constrained by GPS measurements. *Journal of Geophysical Research: Solid Earth*, *110*(B3), 2004JB003209. https://doi.org/10.1029/2004JB003209

Pollitz, F. F. (2003). Transient rheology of the uppermost mantle beneath the Mojave Desert, California. *Earth and Planetary Science Letters*, *215*(1–2), 89–104. https://doi.org/10.1016/S0012-821X(03)00432-1

Pollitz, F. F., & Nyst, M. (2004). A physical model for strain accumulation in the San Francisco Bay Region: The San Francisco Bay Region. *Geophysical Journal International*, *160*(1), 303–318. https://doi.org/10.1111/j.1365-246X.2005.02433.x

Sandwell, D. T., & Wessel, P. (2016). Interpolation of 2-D vector data using constraints from elasticity. *Geophysical Research Letters*, *43*(20). https://doi.org/10.1002/2016GL070340

Savage, J. C., & Burford, R. O. (1973). Geodetic determination of relative plate motion in central California. *Journal of Geophysical Research*, *78*(5), 832–845. https://doi.org/10.1029/JB078i005p00832

Smith, B., & Sandwell, D. (2004). A three-dimensional semianalytic viscoelastic model for time-dependent analyses of the earthquake cycle. *Journal of Geophysical Research: Solid Earth*, *109*(B12), 2004JB003185. https://doi.org/10.1029/2004JB003185

Smith-Konter, B. R., Sandwell, D. T., & Shearer, P. (2011). Locking depths estimated from geodesy and seismology along the San Andreas Fault System: Implications for seismic moment release. *Journal of Geophysical Research*, *116*(B6), B06401. https://doi.org/10.1029/2010JB008117

Sui, S., Shen, W., Holt, W., & Kim, J. (2023). Crustal Architecture Across Southern California and Its Implications on San Andreas Fault Development. *Geophysical Research Letters*, *50*(8), e2022GL101976. https://doi.org/10.1029/2022GL101976

Tong, X., Smith-Konter, B., & Sandwell, D. T. (2014). Is there a discrepancy between geological and geodetic slip rates along the San Andreas Fault System? *Journal of Geophysical Research: Solid Earth*, *119*(3), 2518–2538. https://doi.org/10.1002/2013JB010765

Zeng, Y., & Shen, Z. (2016). A Fault-Based Model for Crustal Deformation, Fault Slip Rates, and Off-Fault Strain Rate in California. *Bulletin of the Seismological Society of America*, *106*(2), 766–784. https://doi.org/10.1785/0120140250

Zeng, Y., & Shen, Z.-K. (2014). Fault network modeling of crustal deformation in California constrained using GPS and geologic observations. *Tectonophysics*, *612–613*, 1–17. https://doi.org/10.1016/j.tecto.2013.11.030